Science Advances
AAAS

advances.sciencemag.org/cgi/content/full/6/21/eaba8404/DC1

Supplementary Materials for

Structural basis for distinct operational modes and protease activation in AAA+ protease Lon

Mia Shin, Cristina Puchades, Ananya Asmita, Neha Puri, Eric Adjei, R. Luke Wiseman, A. Wali Karzai*, Gabriel C. Lander*

*Corresponding author. Email: wali.karzai@stonybrook.edu (A.W.K.); glander@scripps.edu (G.C.L.)

Published 20 May 2020, *Sci. Adv.* **6**, eaba8404 (2020)
DOI: 10.1126/sciadv.aba8404

The PDF file includes:

Other Supplementary Material for this manuscript includes the following:

(available at advances.sciencemag.org/cgi/content/full/6/21/eaba8404/DC1)

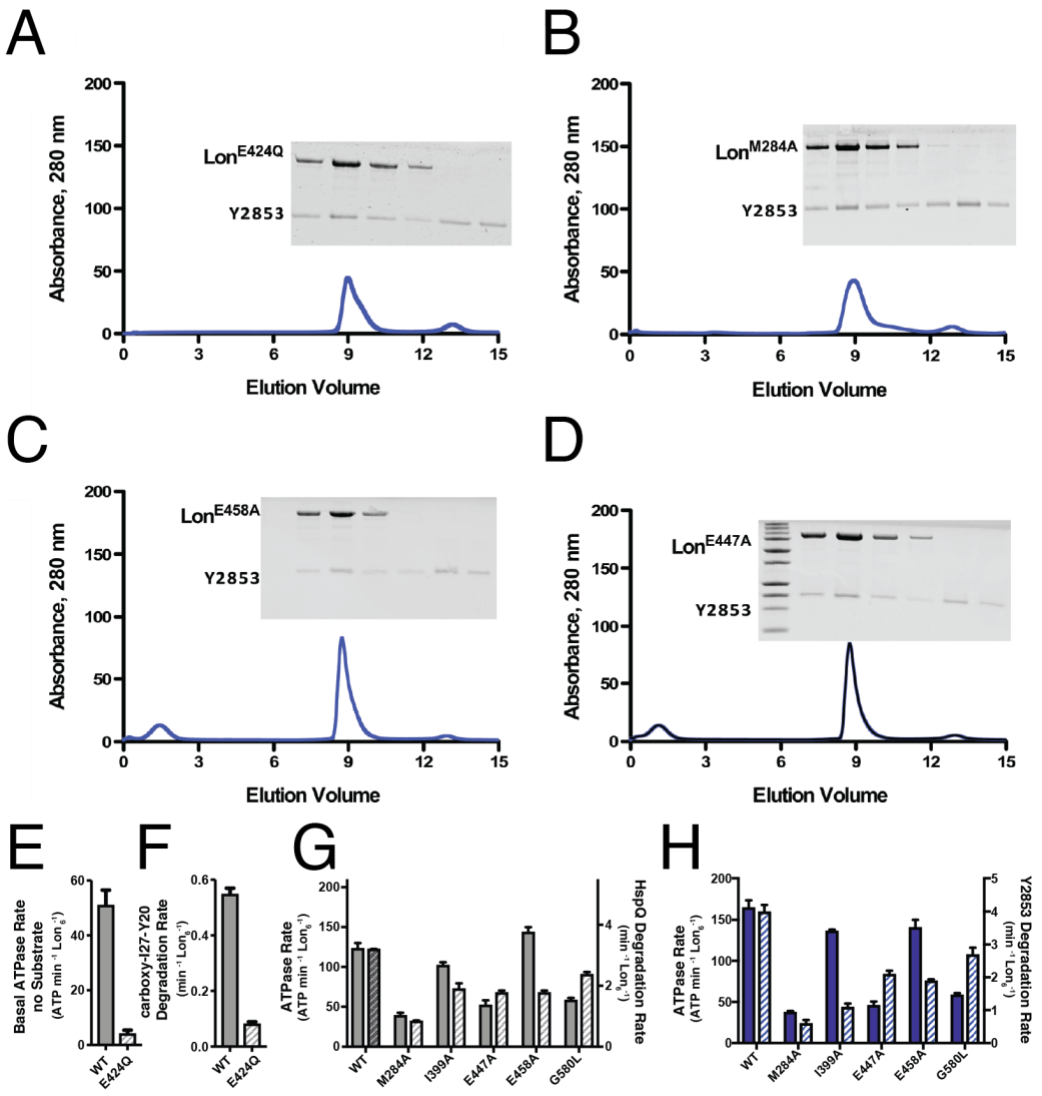

Fig. S1. Purification and biochemical characterization of substrate-bound Lon complexes. Size-exclusion chromatography (SEC) traces showing Y2853 substrate-bound Lon complexes used for structural and biochemical analyses eluting around 9 mL for (**A**) WT Lon bearing a E424Q (Walker B) mutation used for structural studies, (**B**) M284A mutation, (**C**) E458A mutation, and (**D**) E447A mutation, indicating a complex size of ~90 kDa. Overlaid onto traces are SDS-PAGE stained with Coomassie Brilliant Blue showing denatured contents of the elution fractions from the SEC experiment. (**E**) Effect of the slowly hydrolyzing E424Q (Walker B) mutation used for structural studies on basal ATPase rate without substrate and (**F**) degradation of a previously identified substrate, carboxymethylated I27-Y20. (**G-H**) Effect of mutating residues highlighted for the ATPase mechanism for the substrate-bound, “closed” Lon structure on substrate-stimulated ATPase rate (solid bars) and degradation rate of known Lon substrates, HspQ (**G**) and Y2853 (**H**) (hatched bars). Mutated residues include: M284 in NTD_{3H}, I399 in the conserved pore-loop 1, the bridging acidic residue (E447) located at the N-

terminal base of PS1βH, a glutamate residue (E458) at the turn of the PS1βH, and a glycine residue (G580) located in the flexible linker connecting ATPase and protease domains.

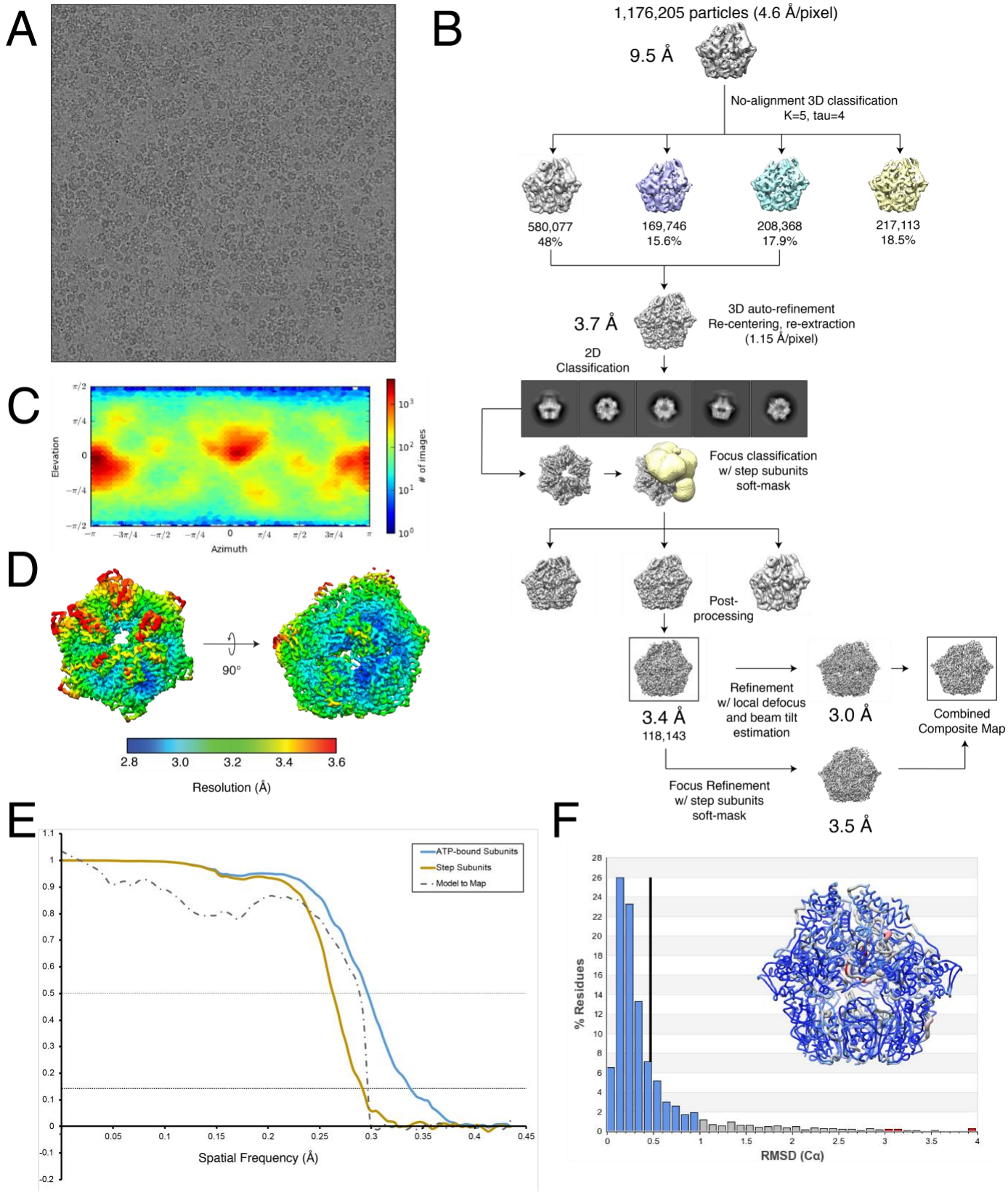

Fig S2. Validation of structural data for substrate-bound, "closed" Lon. (**A**) Representative micrograph from cryo-EM data collection. (**B**) Cryo-EM data processing scheme followed using RELION 2.1b software (*77*) to obtain the final 3D reconstruction of substrate-bound Lon. Final steps included a focused refinement of the final reconstruction using a soft mask around the step subunits and stitching together the focused region with

the remainder of the final map using the “vop maximum” command in UCSF Chimera (*79*). The combined composite map was used for atomic model building and refinement. (**C**) 2-D viewing angle distribution plot of the 118,143 particles used in the final reconstruction. (**D**) Final reconstruction filtered by local resolution calculated using BSOFT (*86*). The final EM density carries a range of resolutions, from 3.4 Å at the core of the complex to > 3.8 Å in more flexible regions such as the step subunits. (**E**) Fourier Shell Correlation (FSC) of the final reconstruction (blue solid line) used to compose four ATP-bound subunits in the combined composite map, the focused refinement map (solid brown line) used to compose two seam subunits in the combined composite map, and the top-refined atomic model vs. the composite combined map (dotted black). (**F**) A histogram showing the per-residue Cα RMSD values calculated from the top 10 refined atomic models using the multi-model pipeline (*84*). A vertical black bar represents the mean per-residue Cα RMSD value, and a worm representation of Lon colored according to the per-residue Cα RMSD values (in Å) is overlaid onto the histogram.

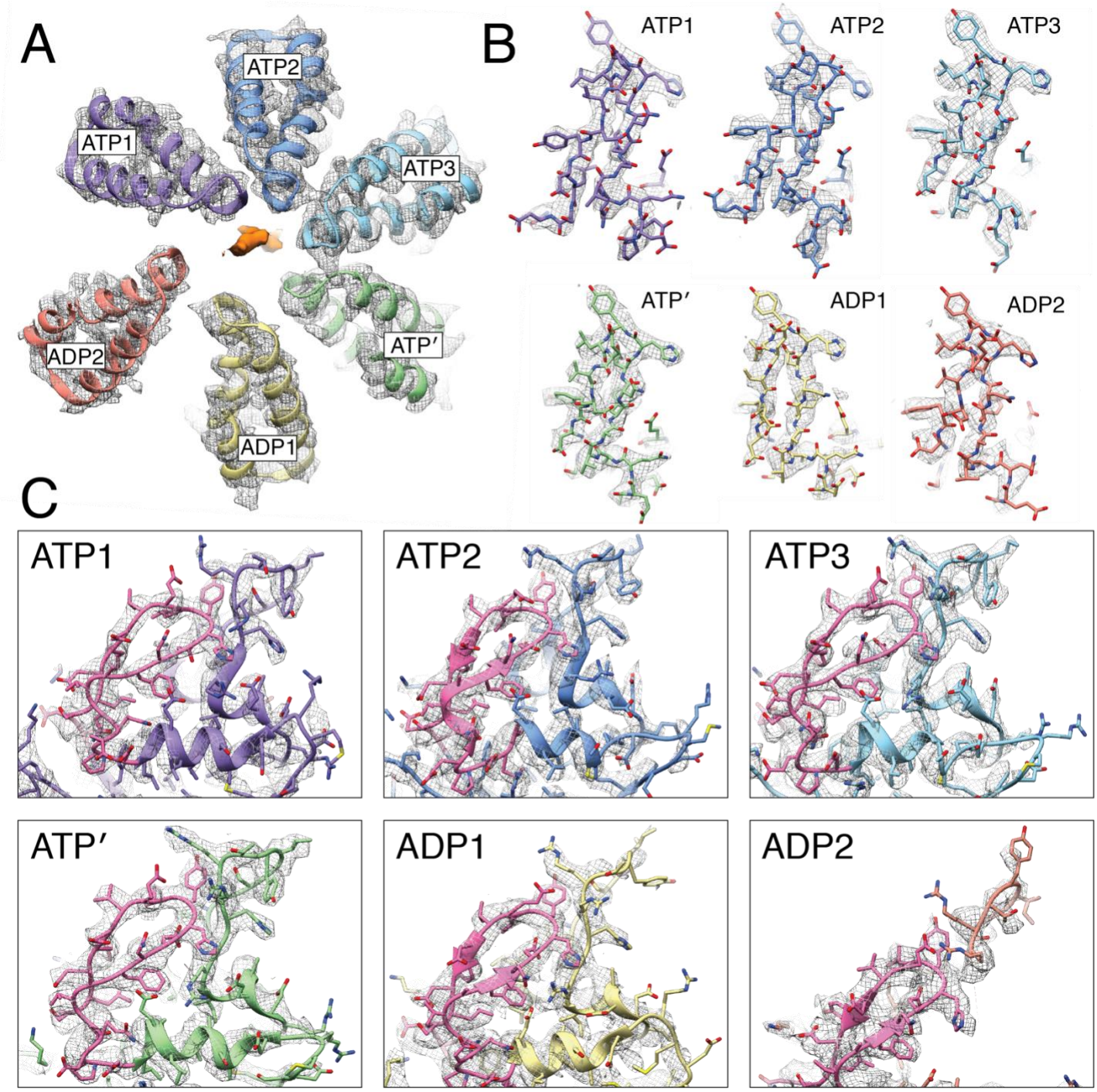

Fig S3. Quality of cryo-EM map for NTD_{3H} and PS1βH in substrate-bound Lon. (**A**) Cryo-EM density and atomic model of the NTD_{3H} subdomains from substrate-bound Lon, colored by subunit as in **Fig. 1**. (**B**) Atomic model of NTD_{3H} subdomain from each of the subunits of substrate-bound Lon is shown in stick representation within the cryo-EM density. (**C**) Atomic model of conserved PS1βH and pore-loop 1 from each of the subunits of substrate-bound Lon shown within the cryo-EM density.

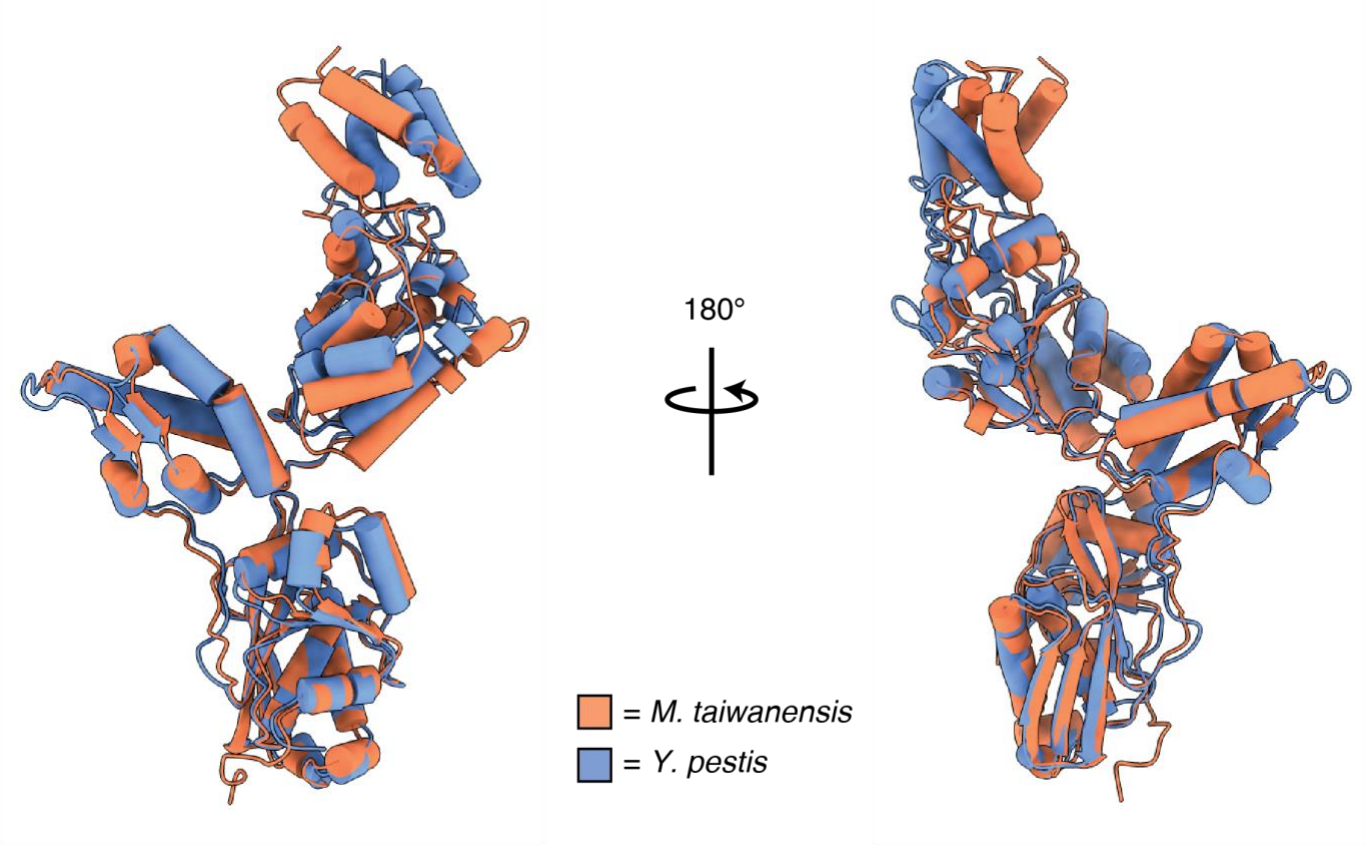

Fig. S4. Secondary structure-based alignment of a single subunit from *M. taiwanensis* and *Y. pestis* Lon. Alignment of the ATP2 subunit with the nucleotide-free protomer structure of a previously determined crystal structure of substrate-free *M. taiwanensis* Lon shows the similarity of the subunit architecture (*41*) (PDB:4YPL). The average Cα RMSD values showed minimal deviations in protease and NTD_{3H} of the two structures (0.777 and 1.011 Å, respectively) whereas the ATPase domains are slightly more variable (1.256 Å). These results show the similarity of the two protomers and consistency of the secondary and tertiary structures of an individual subunit. Higher Cα RMSD values for the ATPase domains are likely due to differences in conformations between a nucleotide and substrate-bound to a nucleotide and substrate-free structure.

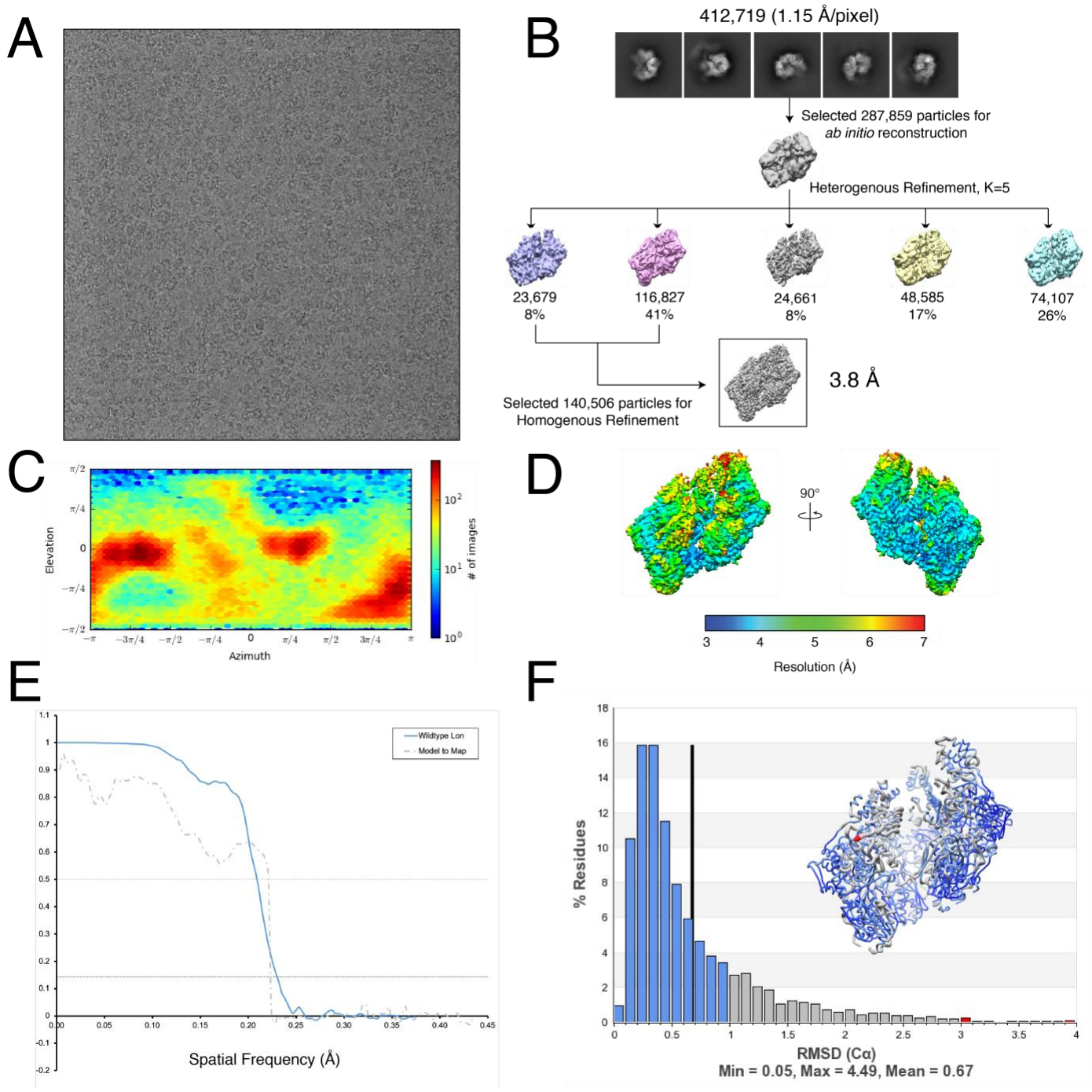

Fig S5. Validation of structural data for substrate-free, "open" Lon. (**A**) Representative micrograph from cryo-EM data collection. (**B**) Cryo-EM data processing scheme followed using cryoSPARC 2.6 software (*76*) to obtain the final 3D reconstruction of substrate-free Lon. (**C**) 2-D viewing angle distribution plot of the 87,738 particles used in the final reconstruction. (**D**) Final reconstruction filtered by local resolution calculated using cryoSPARC. The final EM density carries a range of resolutions, from ~4 Å at the core of the complex to > 6 Å in more flexible regions such as the highest subunit of the open lockwasher configuration. (**E**) Fourier Shell Correlation (FSC) of the final reconstruction (blue solid line) and the top-refined atomic model vs. the final

reconstruction map (dotted black). (**F**) A histogram showing the per-residue Cα RMSD values calculated from the top 10 refined atomic models using the multi-model pipeline (*84*). A vertical black bar represents the mean per-residue Cα RMSD value, and a worm representation of Lon colored according to the per-residue Cα RMSD values (in Å) is overlaid onto the histogram.

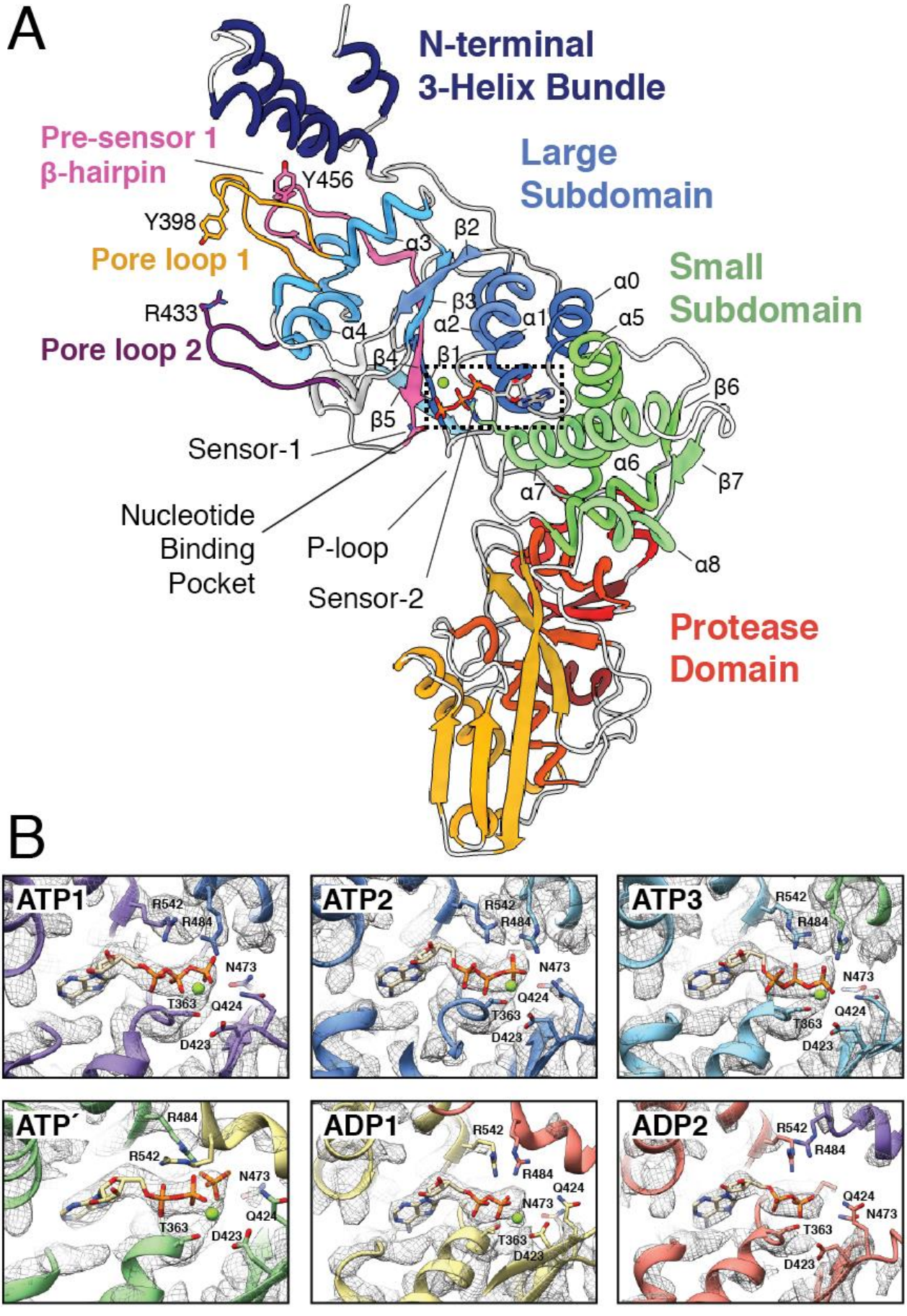
A
N-terminal
3-Helix Bundle
Pre-sensor 1
β-hairpin
Y456
Large
Subdomain
Y398
β2
α3
Pore loop 1
Small
Subdomain
α0
β3
R433
α1
α5
α2
α4
Pore loop 2
β4
β1
β6
β5
Sensor-1
α6
β7
α7
Nucleotide
Binding
Pocket
P-loop
α8
Sensor-2
Protease
Domain
B
ATP1
R542
R484
N473
T363
Q424
D423
ATP2
R542
R484
N473
Q424
T363
D423
ATP3
R542
R484
N473
Q424
T363
D423
ATP´
R484
R542
N473
Q424
T363
D423
ADP1
R542
R484
Q424
N473
T363
D423
ADP2
R542
R484
Q424
N473
T363
D423

Fig. S6. Subunit architecture of substrate-bound Lon protease and distinct nucleotide densities in the nucleotide-binding pocket. (**A**) A Lon protomer, colored by subdomain, with notable and conserved components of the Lon subunit are highlighted and/or labelled. Secondary structural elements of the AAA+ cassette are labelled using the canonical numbering for this domain (*2*). (**B**) Views of the nucleotide binding pockets of all six subunits showing the quality of the cryo-EM density in this region shown using an isosurface mesh representation contoured at a level of sigma = 3.3. The quality of the EM density enables unambiguous assignment of nucleotide state in each of the subunits. ATP1, ATP2, ATP3, and ATP´ subunits possess strong density for nucleotide corresponding to a gamma phosphate-containing nucleotide coordinated by a magnesium cofactor. While the relative positions of the small and large ATPase subdomains of the ATP1, ATP2, and ATP3 subunits are nearly identical, there is a conspicuous 9° compression between the subdomains of the ATP´ subunit (see **fig. S7B**). We thus posit that the ATP´ subunit represents a post-hydrolysis, ADP-Pi intermediate nucleotide state. In contrast, the nucleotide density in the ADP1 and ADP2 subunits corresponded to ADP molecules, as there is no apparent density for gamma phosphates. Notably, the ADP1 subunit contains density corresponding to a magnesium cofactor while ADP2 does not.

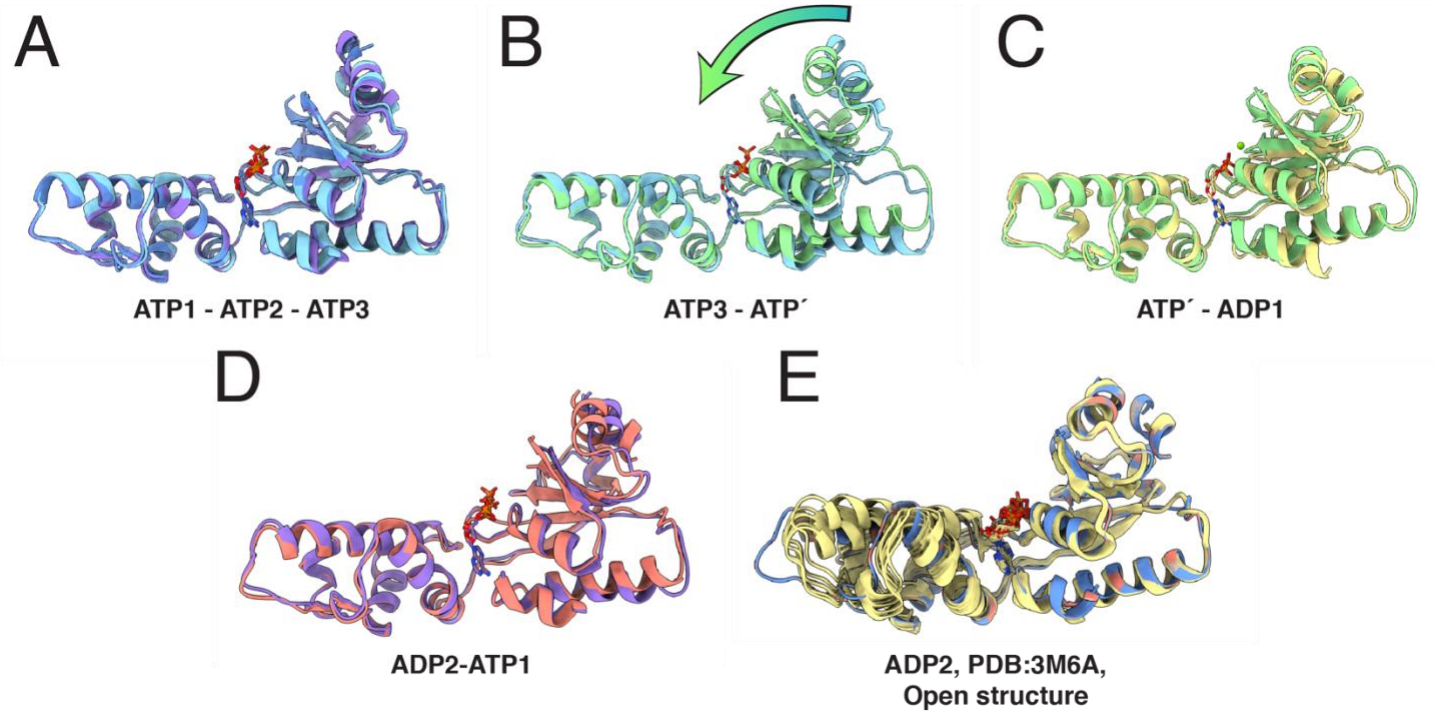

Fig. S7. ATP hydrolysis causes major conformational rearrangements of the ATPase domain in Lon$_{ENZ}$. ATPase subunits of the substrate-bound, Lon$_{ENZ}$ conformer are aligned based on the small ATPase subdomain. (**A**) The three topmost subunits of the ATPase spiral staircase are in similar configurations. (**B**) The ATP´ subunit is in a compressed state, with the ATPase subdomains positioned closer to one another, presumably due to ATP hydrolysis. (**C**) The ADP1 ATPase adopts a similar organization to ATP´ ATPase. (**D**) The ADP2 and ATP1 ATPases are in similar configurations, suggesting that the ADP2 subunit is likely primed for ADP release and ATP re-binding. (**E**) Alignment of the ADP2 subunit of the substrate-bound, Lon$_{ENZ}$ (colored salmon) with the six subunits of the fully ADP-bound *B. subtilis* Lon crystal structure (colored yellow) and the six subunits of the wildtype and substrate-free, Lon$_{OFF}$ cryo-EM structure (colored blue).

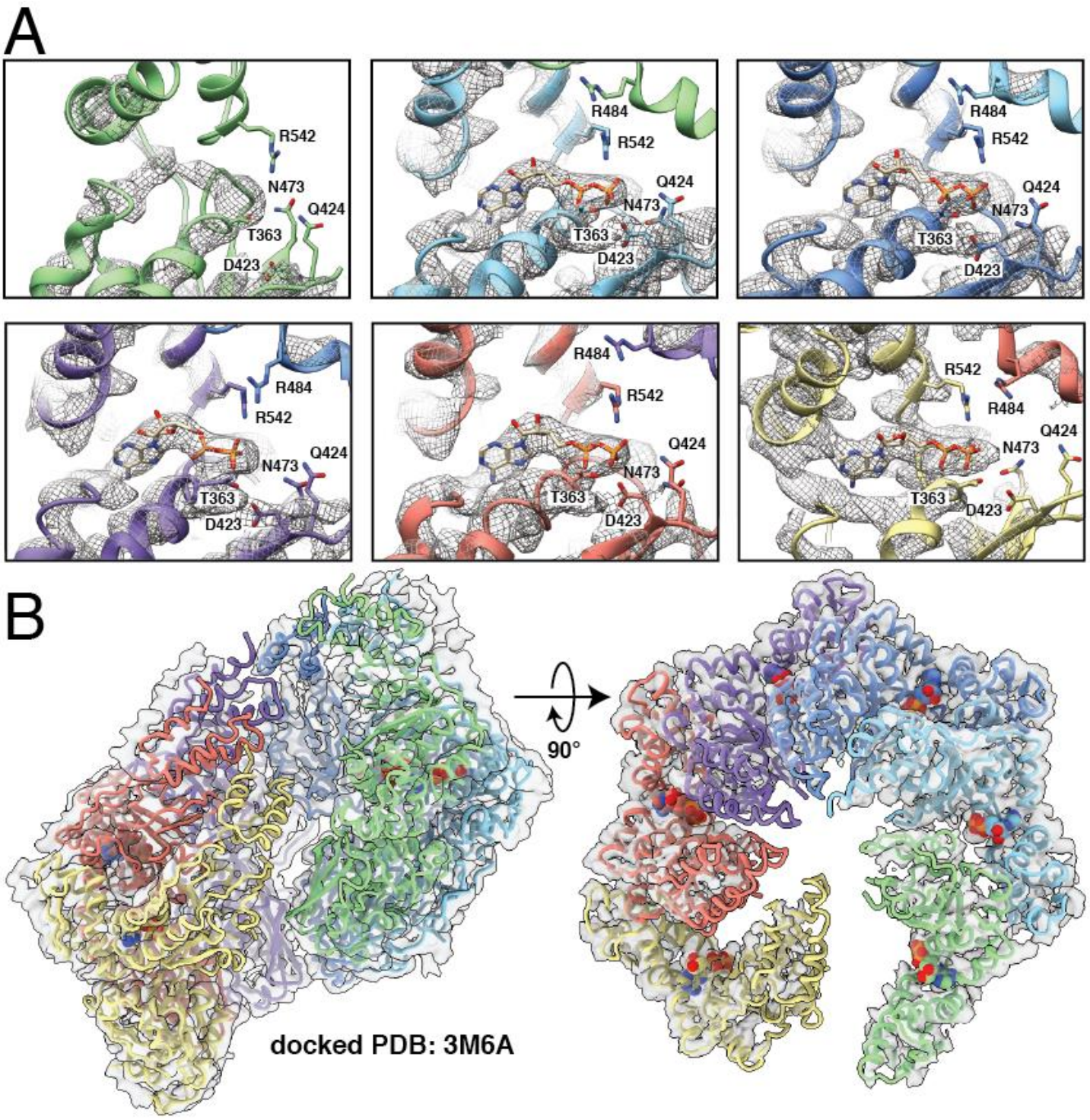

Fig. S8. Structure of substrate-free, Lon$_{OFF}$ structure represents a fully ADP-bound configuration. (**A**) Views of the nucleotide binding pockets of six Lon$_{OFF}$ subunits showing the quality of the cryo-EM density in the region. Cryo-EM density of each subunit is shown using an isosurface mesh representation contoured at a level of sigma = 9.5. The topmost subunit (colored green) has weaker density and thus the nucleotide state of this subunit is ambiguous. However, the quality of the cryo-EM density in the other five subunits enables unambiguous assignment of nucleotide as ADP in each of the subunits. (**B**) The crystal structure of *B. subtilis*

Lon (*42*) (PDB:3M6A) fully bound to ADP is shown docked into cryo-EM map of Lon_{OFF}. Each of the subunits is colored according to the same coloring scheme as in **Fig. 1A**. The fit of the *B. subtilis* Lon structure into our cryo-EM structure supports our conclusion that the substrate-free Lon represents a fully ADP-bound configuration.

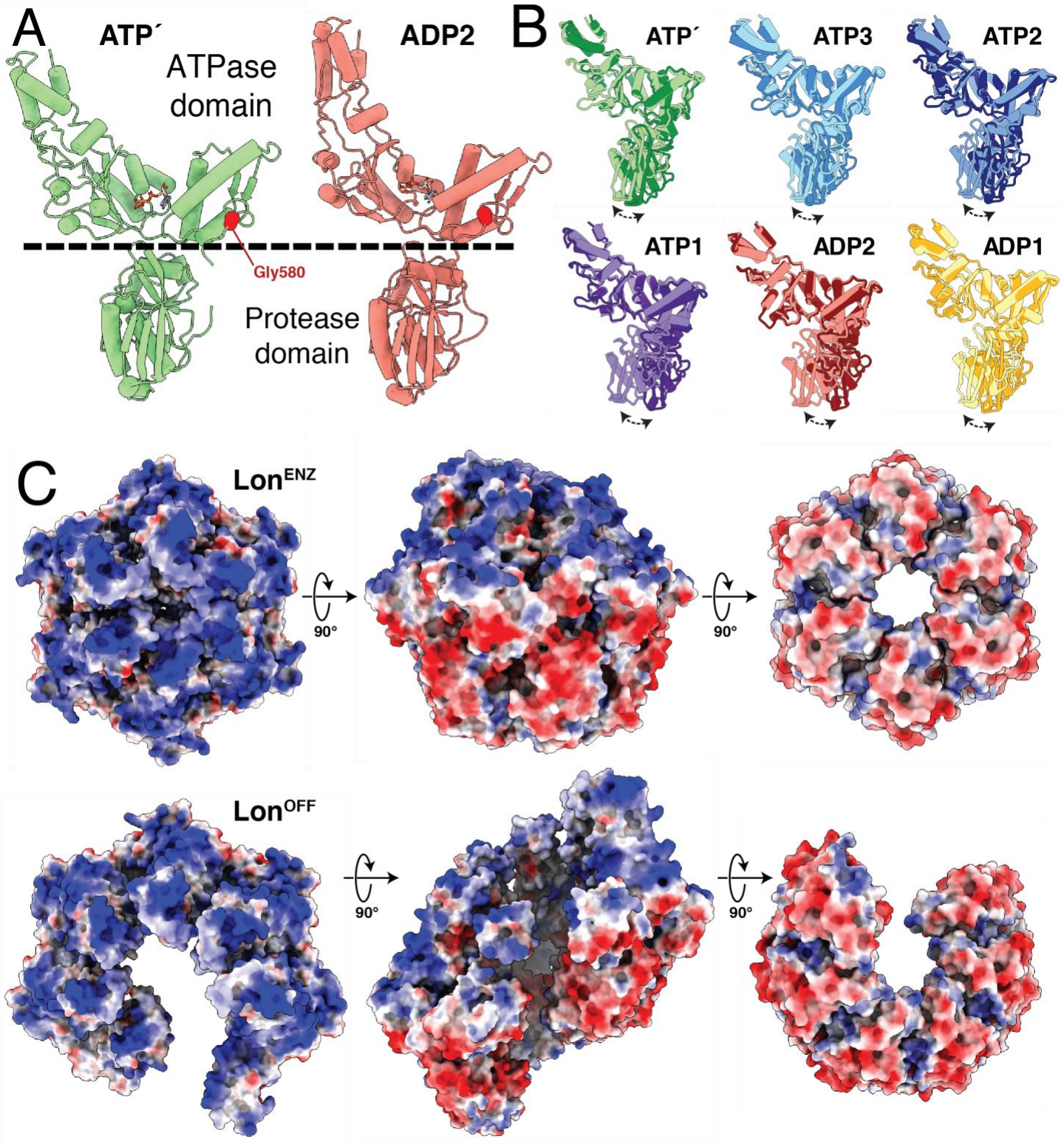

Fig. S9. Protease domains in Lon undergo intra- and inter-subunit conformational changes mediated by a flexible inter-domain linker when transitioning between Lon$_{ENZ}$ and Lon$_{OFF}$ states. (**A**) Side-by-side comparison of ATP´ and ADP2 subunits in the same orientation shows rigid body movements of the ATPase domain between the two subunits while the protease domains remain stable. A glycine residue (G580) in the flexible interdomain linker is highlighted in red. (**B**) Each subunit of the substrate-bound Lon$_{ENZ}$ structure (darker

shaded tube representation) was aligned to the substrate-free Lon_{OFF} structure (lighter shaded tube representation) to emphasize the rotation of the protease domain. These rotations are accommodated in each subunit by a flexible interdomain linker containing G580. (**C**) Electrostatic surface representation of both closed and open Lon structures flanked by orthogonal views of ATPase (left) and protease (right) domains, showing how a large opening in the open lockwasher configuration of Lon breaks polar contacts present in the closed configuration.

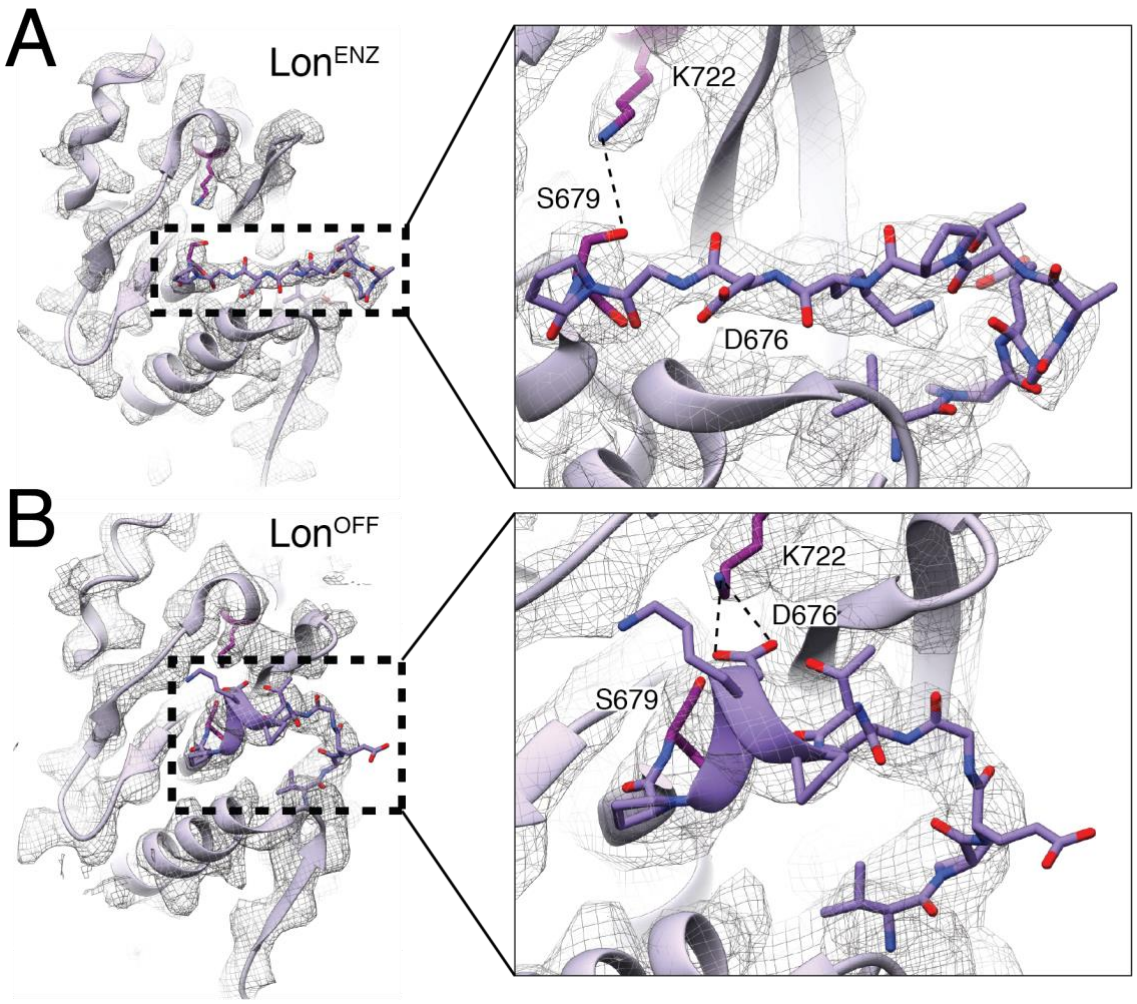

Fig. S10. Quality of cryo-EM map for proteolytic active site for Lon$_{ENZ}$ and Lon$_{OFF}$. (**A**) Cryo-EM density shown as a gray mesh and atomic model of the protease domain from substrate-bound Lon, colored in lavender with important residues highlighted in darker shades of purple. A close-up view of the cryo-EM density of the proteolytic active site is shown to the right, with the atomic model showing the catalytic dyad (magenta) and serine-containing loop (purple stick representation). A hydrogen bond is formed between the two catalytic residues, K722 and S679. (**B**) Cryo-EM density shown as a gray mesh and atomic model of the protease domain from substrate-free Lon, colored in lavender with important residues highlighted in darker shades of purple. A close-up view of the cryo-EM density of the proteolytic active site is shown to the right, with the atomic model showing the catalytic dyad (magenta) that is now obstructed by an aspartic acid residue (D676). Additionally, the serine-containing loop (purple ribbon representation) is now folded into a 3_{10}, sterically occluding the active site and auto-inhibiting the protease domain.

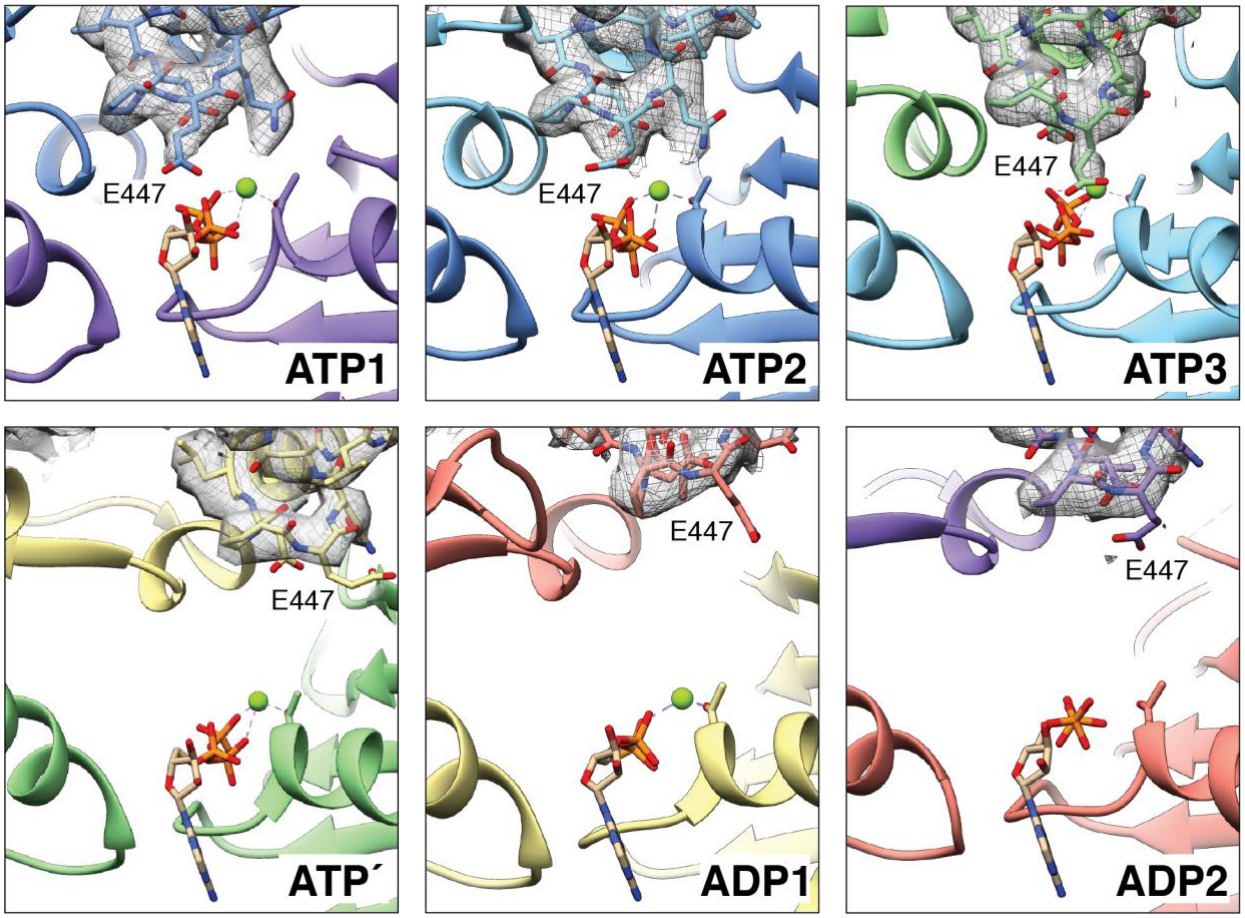

Fig. S11. Quality of cryo-EM map for the trans-acting acidic bridge at the N-terminus of the PS1βH. Cryo-EM density shown in an isosurface mesh representation and atomic model of the ATPase domains from substrate-bound Lon shown as ribbons, colored by subunit as in **Fig. 1**. The nucleotide binding pockets of the post-hydrolysis subunits (ATP´, ADP1, and ADP2) have weaker density for the key glutamate (E447) from the clockwise neighboring subunit and thus the rotamer assignment of this residue is ambiguous although the chain trace of the PS1βH was built *de novo* into the map with a high level of confidence. However, the quality of the cryo-EM density in the other three ATP-bound subunits enables unambiguous rotamer assignment of this residue.

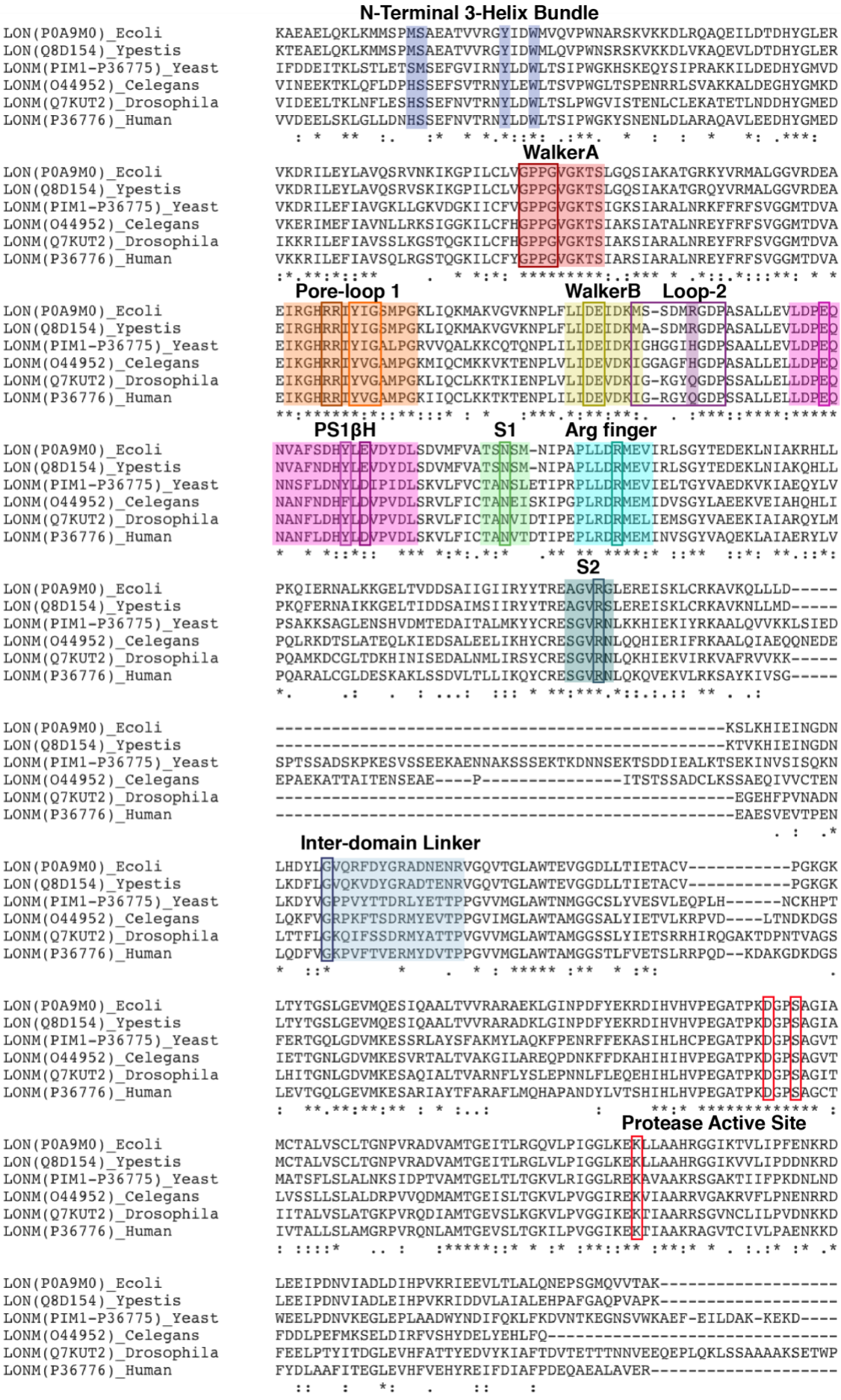
N-Terminal 3-Helix Bundle
WalkerA
Pore-loop 1
WalkerB
Loop-2
PS1βH
S1
Arg finger
S2
Inter-domain Linker
Protease Active Site
LON(P0A9M0)_Ecoli
LON(Q8D154)_Ypestis
LONM(PIM1-P36775)_Yeast
LONM(O44952)_Celegans
LONM(Q7KUT2)_Drosophila
LONM(P36776)_Human

Fig. S12. Conservation of ATPase allostery and protease inactivation mechanisms across Lon proteases. Clustal W alignment of the Uniprot sequences of the NTD_{3H} and ATPase domains of Lon homologs, including cytoplasmic *E. coli* and *Y. pestis* Lon and mitochondrial Lon from yeast (Pim1), *C. elegans*, *Drosophila melanogaster*, and humans. This alignment suggests strict mechanistic conservation amongst Lon proteins in diverse model organisms and environments, as we found all key residues identified in our structure to be strictly conserved in all sequences studied: the N-terminal 3-Helix Bundle (M294, S285, Y294, and W297 in light blue), P-loop (purple box), pore-loop 1 aromatic-hydrophobic residues (pink box), coordinating acidic residues in the Walker B motif (dark blue box), pre-sensor 1 beta hairpin insertion with conserved residues E447, Y456, and E458 in boxes, sensor-1, a trans-acting arginine finger (maroon box), as well as a cis-acting arginine finger present in sensor-2 (green). Additionally, the aspartic acid residue (D676) critical in the protease inactivation mechanism upon transitioning between Lon_{ON} and Lon_{OFF} states is conserved across Lon proteases.

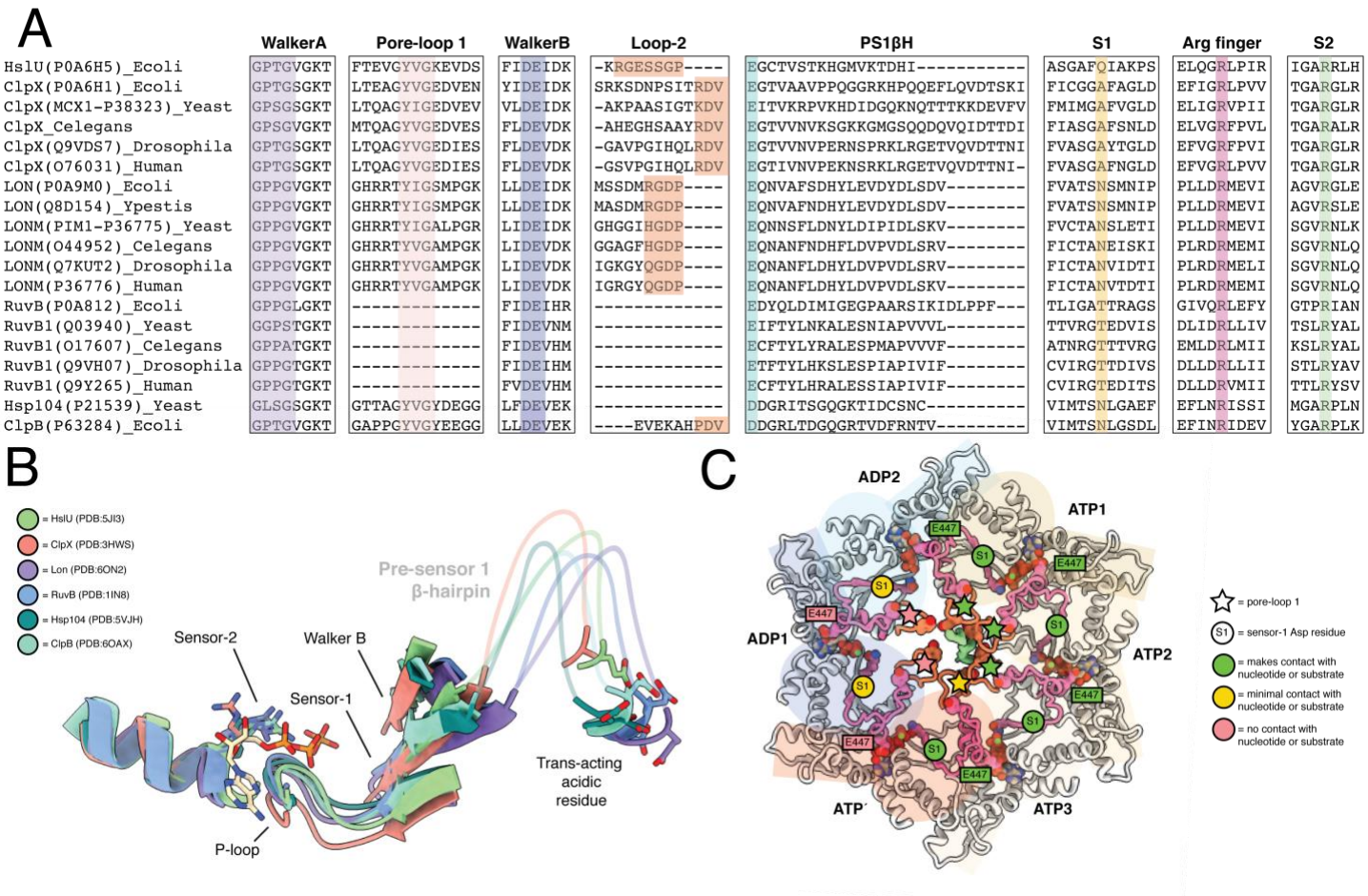

Fig. S13. Conservation of allosteric mechanism across HCLR clade proteins. (**A**) Alignment of conserved regions in the AAA+ domains of HCLR clade proteins: HslU, ClpX, Lon, RuvB, Hsp104, and ClpB. This alignment suggests mechanistic conservation amongst HCLR clade proteins, as we found all key residues identified in our structure to be strictly conserved in all sequences studied: P-loop (purple in Walker A motif), pore-loop 1 aromatic-hydrophobic residues in protein translocases (pink), coordinating acidic residues in the Walker B motif (blue) a pre-sensor 1 beta hairpin insertion with a trans-acting glutamate residue (teal) at its N-terminus, sensor-1 (yellow), a trans-acting arginine finger (maroon), as well as a cis-acting arginine finger in sensor-2 (green). (**B**) Structural conservation of essential elements of the proposed allosteric mechanism amongst HCLR clade proteins, including HslU (PDB:5JI3), ClpX (PDB:3HWS), Lon (PDB:6ON2), RuvB (PDB:1IN8), Hsp104 (PDB:5VJH), and ClpB (PDB:6OAX). (**C**) A top view of the substrate-bound Lon with each ATPase domain highlighted by an ellipse and rectangle on the large and small subdomains, respectively. Key structural elements are highlighted in hot pink: residues that comprise the pore-loop 1, PS1ßH, sensor-1, and a trans-acting glutamate residue. The mechanism of allostery in Lon involving these shared elements is likely conserved across all HCLR clade proteins.

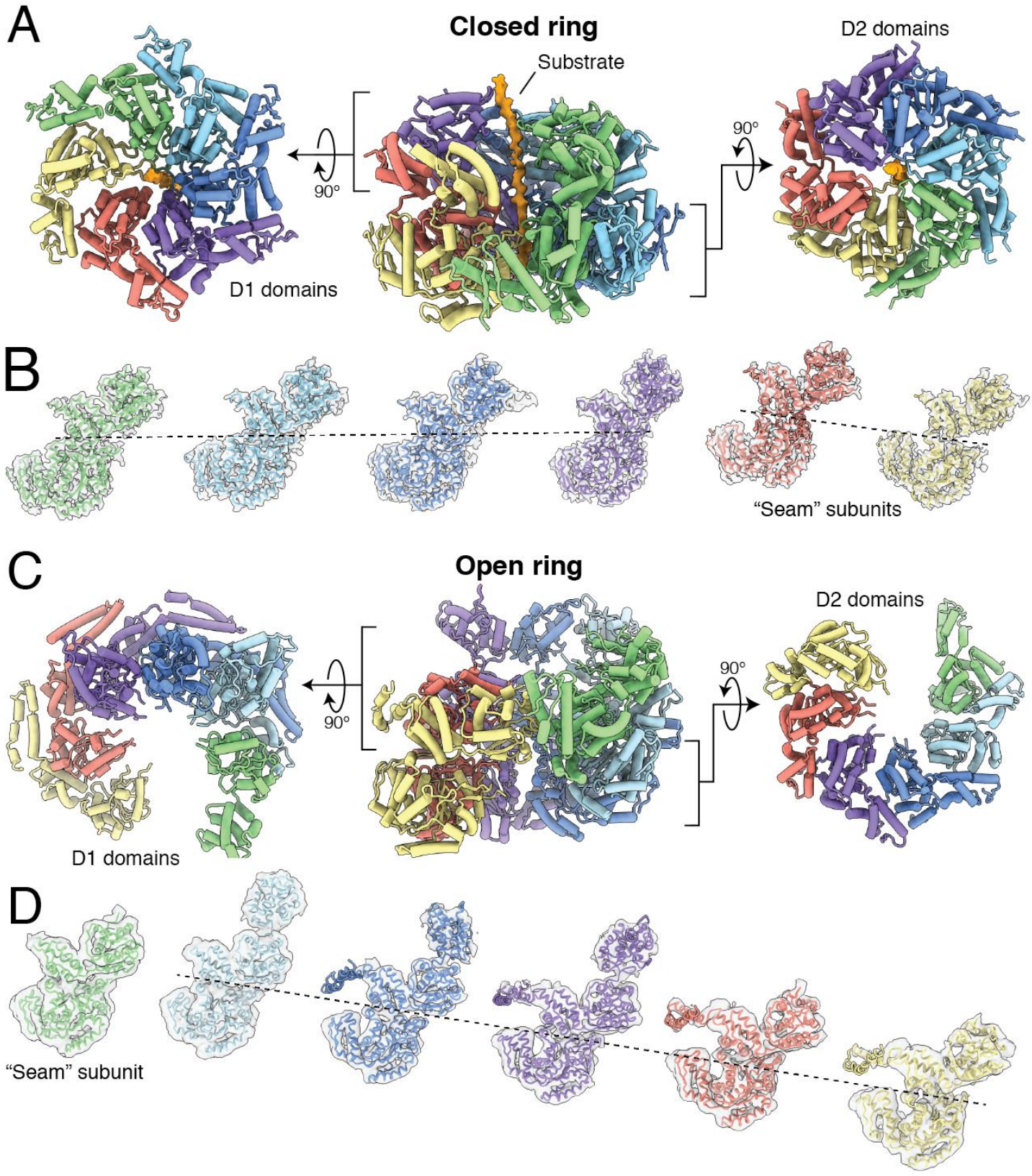

Fig. S14. Architectures of the substrate-bound, "closed" and substrate-free, "open" Hsp104 configurations. (**A**) Cutaway view of the substrate-bound *S. cerevisiae Hsp*104 atomic model (*9*) (PDB:5VJH) (center) flanked by orthogonal views of the ATPase D1 (left) and D2 (right) domain rings. Cryo-EM density for

substrate is colored orange while each subunit of the homohexamer is assigned a color depending on its position in the spiral staircase. (**B**) Each of the protomers of the substrate-bound structure are shown in the same orientation based on the position of the D2 domain. The descending and ascending movements of the subunits are accentuated by dotted lines running through the inter-domain linker. (**C**) Cutaway view of the substrate-free *S. cerevisiae* Hsp104 (*60*) (PDB:5KNE) (center) flanked by orthogonal views of the ATPase D1 (left) and D2 (right) domain rings. Each subunit of the "open" homohexamer is assigned a color that correlates with the subunit's position in the closed spiral staircase architecture. (**D**) Individual protomers of the substrate-free structure oriented in the same direction, lined up side-by-side. The descending movement of the subunits is accentuated by a dotted line running through the inter-domain linker. These results show striking resemblance to the closed, substrate-bound and open, substrate-free cryo-EM structures of *Y. pestis* Lon protease shown in **Fig. 1**, suggesting conservation of conformational switching to access distinct functional modalities across AAA+ protein translocases.

Movie S1. Mechanism of substrate translocation by the Lon protease. A low-resolution surface representation of the large and small ATPase subdomains is shown to emphasize the movements associated with ATP-dependent substrate translocation. Subunits colored yellow correspond to the uppermost ATP-bound protomers of the spiral staircase, the subunit colored red corresponds to the ATP´ subunit, and the subunits colored blue correspond to the ADP-bound seam subunits. Nucleotides are represented by large spheres (ATP, ATP´, and ADP colored orange, magenta, and blue, respectively). Substrate is colored with alternating residues colored light and dark green.

Movie S2. Mechanism of Lon protease activation upon transition between Lon_{OFF} and Lon_{ENZ} conformations. A linear interpolation between the aligned protease domains of Lon_{OFF} and Lon_{ENZ} shows the mechanism by which Lon regulates proteolytic activity in both states. Atomic models are shown using a ribbon representation overlaid with a low-resolution surface representation of the protease domains in both Lon_{OFF} and Lon_{ENZ} structures. In the Lon_{OFF} conformer, the S679-containing loop (residues 673-677) folds into a 3_{10} helix that sterically occludes substrates from accessing the proteolytic active site. Additionally, an aspartic acid residue within this helix (D676) forms a hydrogen bond with K722, inhibiting catalytic dyad formation between S679 and K722. Upon substrate binding and nucleotide exchange, Lon_{OFF} undergoes a large conformational change to form Lon_{ENZ}, symmetrizing the protease domains. Upon this conformational change, the S679-containing loop extends towards the neighboring subunit, where it is stabilized by inter-subunit interactions with conserved residues V633, P678, and E706. Additionally, D676 likely stabilizes the extended loop's position through intra-subunit hydrogen-bonding interactions with backbone atoms of residues E632 and V633. This extended loop establishes a substrate-binding groove that positions targeted peptides into the proteolytic active site for cleavage. *E. coli* Lon (green ribbon) bound to Bortezomib (orange stick representation) (PDB:47PN) (*57*) is shown aligned with Lon_{ENZ} to indicate how an unfolded substrate (orange) might be positioned in this substrate-binding groove for cleavage.

Movie S3. Mechanism of substrate engagement, translocation, and release in Lon protease. The substrate processing mechanism is summarized using a low-resolution envelope of Lon to emphasize the motions involved in the switch between operational modes. In the absence of substrate, the Lon protease is organized into a left-

handed open lockwasher configuration (Lon_{OFF}). ADP is bound in all nucleotide binding pockets, with the exception of the uppermost subunit, whose nucleotide binding pocket is exposed and able to undergo nucleotide exchange. Simultaneous binding of substrate and ATP triggers a rearrangement to the Lon_{ENZ} conformation, leading to sequential ADP to ATP exchange as pore-loop residues in three additional subunits progressively engage substrate and the closed ring conformer is adopted. An ATP hydrolysis event in the lowest ATP-bound subunit “locks” Lon into a substrate-bound, proteolytically active conformation (Lon_{ENZ}). As a result of this conformational switch, the first subunit to engage substrate, which was positioned the uppermost position in Lon_{OFF}, is now positioned at the bottom of the ATPase ring in Lon_{ENZ}. A single hydrolysis event can in this way translocate substrate a length of eight residues, securely positioning the substrate peptide in the center of the ATPase channel. The Lon_{ENZ} conformer then translocates substrate a length of two amino acids per ATP hydrolysis event. When Lon_{ENZ} reaches the end of the substrate or encounters a tightly folded region, the pore-loop of the upper-most subunit can no longer engage a span of unfolded peptide, so that this subunit will remain in an ADP-bound state while ATP hydrolysis and translocation continues in the remaining ATP-bound subunits. However, after each hydrolysis and translocation event, ADP will no longer be exchanged for ATP, resulting in a return to the Lon_{OFF} conformer. Unprocessed substrate is able to leave through the lateral opening in Lon_{OFF}.

Table S1. CryoEM data collection, refinement, and validation statistics

Sample, EMDB / PDB ID	**Lon_{WB}, 20133 / 6ON2**	**Lon_{WT}, 21009 / 6V11**
Data collection		
Microscope	Talos Arctica	Talos Arctica
Voltage (keV)	200	200
Detector	K2 Summit	K2 Summit
Magnification (nominal)	36,000X	36,000X
Magnification (calibrated)	43,478X	43,478X
Exposure navigation	Image Shift	Image Shift
Data acquisition software	Leginon (*69*)	Leginon (*69*)
Total electron exposure (e-/Å$_2$)	52	50
Exposure rate (e-/pixel/sec)	5.3	5.7
Number of frames	44	58
Pixel size (Å)	1.15	1.15
Defocus range (μm)	-0.8 to -1.2	-0.8 to -1.5
Micrographs collected	4071	1864
Reconstruction		
Micrographs used	4071	1864
Total extracted particles (no.)	1,176,206	412,719
Refined particles	1,176,206	412,719
Final particles (no.)	118,143	140,506
Symmetry imposed	C1	C1
Resolution (global)		
FSC 0.5	4.2 Å (unmasked) ATP1-ATP´ (masked): 3.3 Å ADP1-ADP2 (masked): 3.8 Å	8.6 Å (unmasked) 4.8 Å (masked)
FSC 0.143	3.5 Å (unmasked) ATP1-ATP´ (masked): 3.0 Å ADP1-ADP2 (masked): 3.5 Å	4.6 Å (unmasked) 3.8 Å (masked)
Resolution range (local)	3.4 – 4.2 Å	3.0 – 7.0 Å
Applied B-factor (Å$_2$)	-52	-115
Model Composition		
Protein residues	3,146	2,912
Ligands	6	5
Model Refinement		
Refinement package	Phenix (*83*)	Phenix (*83*)
Map Correlation Coefficient		
Local	0.80	0.80
R.m.s. deviations from ideal values		
Bond lengths	0.01	0.01
Bond angles (°)	0.83	1.02
Validation		
Ramachandran (%)		
Outliers	0.00	0.00
Allowed	4.08	8.16
Favored	95.92	91.84
MolProbity score	1.55	1.89
Poor rotamers (%)	0.08	0.98%
Clashscore (all atoms)	5.09	7.33
C-beta deviations	0	0
Mean per-residue Ca RMSD (Å)	0.46	0.67
Per-residue Ca RMSD range (Å)	0.03 – 5.32	0.05 – 4.49
CaBLAM Outliers (*87*)	2.24%	3.67%
EMRinger Score (*88*)	3.17	1.63

REFERENCES AND NOTES

1. J. P. Erzberger, J. M. Berger, Evolutionary relationships and structural mechanisms of AAA+ proteins. *Annu. Rev. Biophys. Biomol. Struct.* **35**, 93–114 (2006).

2. P. I. Hanson, S. W. Whiteheart, AAA+ proteins: Have engine, will work. *Nat. Rev. Mol. Cell Biol.* **6**, 519–529 (2005).

3. L. M. Iyer, D. D. Leipe, E. V. Koonin, L. Aravind, Evolutionary history and higher order classification of AAA+ ATPases. *J. Struct. Biol.* **146**, 11–31 (2004).

4. R. T. Sauer, T. A. Baker, AAA+ proteases: ATP-fueled machines of protein destruction. *Annu. Rev. Biochem.* **80**, 587–612 (2011).

5. S. N. Gates, A. Martin, Stairway to translocation: AAA+ motor structures reveal the mechanisms of ATP-dependent substrate translocation. *Protein Sci.* **29**, 407–419 (2019).

6. C. Puchades, C. R. Sandate, G. C. Lander, The molecular principles governing the activity and functional diversity of AAA+ proteins. *Nat. Rev. Mol. Cell Biol.* **21**, 43–58 (2020).

7. I. Cooney, H. Han, M. G. Stewart, R. H. Carson, D. T. Hansen, J. H. Iwasa, J. C. Price, C. P. Hill, P. S. Shen, Structure of the Cdc48 segregase in the act of unfolding an authentic substrate. *Science* **365**, 502–505 (2019).

8. A. H. de la Peña, E. A. Goodall, S. N. Gates, G. C. Lander, A. Martin, Substrate-engaged 26*S* proteasome structures reveal mechanisms for ATP-hydrolysis–driven translocation. *Science* **362**, eaav0725 (2018).

9. S. N. Gates, A. L. Yokom, J. Lin, M. E. Jackrel, A. N. Rizo, N. M. Kendsersky, C. E. Buell, E. A. Sweeny, K. L. Mack, E. Chuang, M. P. Torrente, M. Su, J. Shorter, D. R. Southworth, Ratchet-like polypeptide translocation mechanism of the AAA+ disaggregase Hsp104. *Science* **357**, 273–279 (2017).

10. H. Han, N. Monroe, W. I. Sundquist, P. S. Shen, C. P. Hill, The AAA ATPase Vps4 binds ESCRT-III substrates through a repeating array of dipeptide-binding pockets. *eLife* **6**, e31324 (2017).

11. N. Monroe, H. Han, P. S. Shen, W. I. Sundquist, C. P. Hill, Structural basis of protein translocation by the Vps4-Vta1 AAA ATPase. *eLife* **6**, e24487 (2017).

12. C. Puchades, B. Ding, A. Song, R. L. Wiseman, G. C. Lander, S. E. Glynn, Unique structural features of the mitochondrial AAA+ protease AFG3L2 reveal the molecular basis for activity in health and disease. *Mol. Cell* **75**, 1073–1085.e6 (2019).

13. C. Puchades, A. J. Rampello, M. Shin, C. J. Giuliano, R. L. Wiseman, S. E. Glynn, G. C. Lander, Structure of the mitochondrial inner membrane AAA+ protease YME1 gives insight into substrate processing. *Science* **358**, eaao0464 (2017).

14. Z. A. Ripstein, R. Huang, R. Augustyniak, L. E. Kay, J. L. Rubinstein, Structure of a AAA+ unfoldase in the process of unfolding substrate. *eLife* **6**, e25754 (2017).

15. A. N. Rizo, J. Lin, S. N. Gates, E. Tse, S. M. Bart, L. M. Castellano, F. DiMaio, J. Shorter, D. R. Southworth, Structural basis for substrate gripping and translocation by the ClpB AAA+ disaggregase. *Nat. Commun.* **10**, 2393 (2019).

16. E. C. Twomey, Z. Ji, T. E. Wales, N. O. Bodnar, S. B. Ficarro, J. A. Marto, J. R. Engen, T. A. Rapoport, Substrate processing by the Cdc48 ATPase complex is initiated by ubiquitin unfolding. *Science* **365**, eaax1033 (2019).

17. K. I. White, M. Zhao, U. B. Choi, R. A. Pfuetzner, A. T. Brunger, Structural principles of SNARE complex recognition by the AAA+ protein NSF. *eLife* **7**, e38888 (2018).

18. H. Yu, T. J. Lupoli, A. Kovach, X. Meng, G. Zhao, C. F. Nathan, H. Li, ATP hydrolysis-coupled peptide translocation mechanism of *Mycobacterium tuberculosis* ClpB. *Proc. Natl. Acad. Sci. U.S.A.* **115**, E9560–E9569 (2018).

19. F. Beck, P. Unverdorben, S. Bohn, A. Schweitzer, G. Pfeifer, E. Sakata, S. Nickell, J. M. Plitzko, E. Villa, W. Baumeister, F. Förster, Near-atomic resolution structural model of the yeast 26S proteasome. *Proc. Natl. Acad. Sci. U.S.A.* **109**, 14870–14875 (2012).

20. S. Chen, J. Wu, Y. Lu, Y.-B. Ma, B.-H. Lee, Z. Yu, Q. Ouyang, D. J. Finley, M. W. Kirschner, Y. Mao, Structural basis for dynamic regulation of the human 26S proteasome. *Proc. Natl. Acad. Sci. U.S.A.* **113**, 12991–12996 (2016).

21. P. Śledź, P. Unverdorben, F. Beck, G. Pfeifer, A. Schweitzer, F. Förster, W. Baumeister, Structure of the 26S proteasome with ATP-γS bound provides insights into the mechanism of nucleotide-dependent substrate translocation. *Proc. Natl. Acad. Sci. U.S.A.* **110**, 7264–7269 (2013).

22. X. Fei, T. A. Bell, S. Jenni, B. M. Stinson, T. A. Baker, S. C. Harrison, R. T. Sauer, Structures of the ATP-fueled ClpXP proteolytic machine bound to protein substrate. *eLife* **9**, e52774 (2020).

23. K. E. Lopez, A. N. Rizo, E. Tse, J. Lin, N. W. Scull, A. C. Thwin, A. L. Lucius, J. Shorter, D. R. Southworth, Conformational plasticity of the ClpAP AAA+ protease couples protein unfolding and proteolysis. *bioRxiv*, 820209 (2019).

24. Z. A. Ripstein, S. Vahidi, W. A. Houry, J. L. Rubinstein, L. E. Kay, A processive rotary mechanism couples substrate unfolding and proteolysis in the ClpXP degradation machinery. *eLife* **9**, e52158 (2020).

25. M.-E. Aubin-Tam, A. O. Olivares, R. T. Sauer, T. A. Baker, M. J. Lang, Single-molecule protein unfolding and translocation by an ATP-fueled proteolytic machine. *Cell* **145**, 257–267 (2011).

26. J. C. Cordova, A. O. Olivares, Y. Shin, B. M. Stinson, S. Calmat, K. R. Schmitz, M.-E. Aubin-Tam, T. A. Baker, M. J. Lang, R. T. Sauer, Stochastic but highly coordinated protein unfolding and translocation by the ClpXP proteolytic machine. *Cell* **158**, 647–658 (2014).

27. R. A. Maillard, G. Chistol, M. Sen, M. Righini, J. Tan, C. M. Kaiser, C. Hodges, A. Martin, C. Bustamante, ClpX(P) generates mechanical force to unfold and translocate its protein substrates. *Cell* **145**, 459–469 (2011).

28. A. Martin, T. A. Baker, R. T. Sauer, Rebuilt AAA + motors reveal operating principles for ATP-fuelled machines. *Nature* **437**, 1115–1120 (2005).

29. P. Rodriguez-Aliaga, L. Ramirez, F. Kim, C. Bustamante, A. Martin, Substrate-translocating loops regulate mechanochemical coupling and power production in AAA+ protease ClpXP. *Nat. Struct. Mol. Biol.* **23**, 974–981 (2016).

30. M. Sen, R. A. Maillard, K. Nyquist, P. Rodriguez-Aliaga, S. Pressé, A. Martin, C. Bustamante, The ClpXP protease unfolds substrates using a constant rate of pulling but different gears. *Cell* **155**, 636–646 (2013).

31. M. J. Baker, T. Tatsuta, T. Langer, Quality control of mitochondrial proteostasis. *Cold Spring Harb. Perspect. Biol.* **3**, a007559 (2011).

32. I. Lee, C. K. Suzuki, Functional mechanics of the ATP-dependent Lon protease- lessons from endogenous protein and synthetic peptide substrates. *Biochim. Biophys. Acta* **1784**, 727–735 (2008).

33. M. Pinti, L. Gibellini, M. Nasi, S. De Biasi, C. A. Bortolotti, A. Iannone, A. Cossarizza, Emerging role of Lon protease as a master regulator of mitochondrial functions. *Biochim. Biophys. Acta* **1857**, 1300–1306 (2016).

34. P. M. Quiros, T. Langer, C. Lopez-Otin, New roles for mitochondrial proteases in health, ageing and disease. *Nat. Rev. Mol. Cell Biol.* **16**, 345–359 (2015).

35. I. Lee, A. J. Berdis, C. K. Suzuki, Recent developments in the mechanistic enzymology of the ATP-dependent Lon protease from Escherichia coli: Highlights from kinetic studies. *Mol. Biosyst.* **2**, 477–483 (2006).

36. E. Culp, G. D. Wright, Bacterial proteases, untapped antimicrobial drug targets. *J. Antibiot.* **70**, 366–377 (2017).

37. I. Botos, E. E. Melnikov, S. Cherry, J. E. Tropea, A. G. Khalatova, F. Rasulova, Z. Dauter, M. R. Maurizi, T. V. Rotanova, A. Wlodawer, A. Gustchina, The catalytic domain of Escherichia coli Lon protease has a unique fold and a Ser-Lys dyad in the active site. *J. Biol. Chem.* **279**, 8140–8148 (2004).

38. E. Gur, R. T. Sauer, Degrons in protein substrates program the speed and operating efficiency of the AAA+ Lon proteolytic machine. *Proc. Natl. Acad. Sci. U.S.A.* **106**, 18503–18508 (2009).

39. S. C. Park, B. Jia, J. K. Yang, D. L. Van, Y. G. Shao, S. W. Han, Y. J. Jeon, C. H. Chung, G. W. Cheong, Oligomeric structure of the ATP-dependent protease La (Lon) of Escherichia coli. *Mol. Cells* **21**, 129–134 (2006).

40. E. F. Vieux, M. L. Wohlever, J. Z. Chen, R. T. Sauer, T. A. Baker, Distinct quaternary structures of the AAA+ Lon protease control substrate degradation. *Proc. Natl. Acad. Sci. U.S.A.* **110**, E2002–E2008 (2013).

41. C. C. Lin, S. C. Su, M. Y. Su, P. H. Liang, C. C. Feng, S. H. Wu, C. I. Chang, Structural insights into the allosteric operation of the Lon AAA+ protease. *Structure* **24**, 667–675 (2016).

42. R. E. Duman, J. Löwe, Crystal structures of Bacillus subtilis Lon protease. *J. Mol. Biol.* **401**, 653–670 (2010).

43. I. Botos, G. T. Loutos, W. Wu, S. Cherry, R. Ghirlando, A. M. Kudhaev, J. E. Tropea, A. Gustchina, A. Wlodawer, Cryo-EM structure of substrate-free *E. coli* Lon protease provides insights into the dynamics of Lon machinery. *Curr. Res. Struct. Biol.* **1**, 13–20 (2019).

44. C. M. Ho, J. R. Beck, M. Lai, Y. Cui, D. E. Goldberg, P. F. Egea, Z. H. Zhou, Malaria parasite translocon structure and mechanism of effector export. *Nature* **561**, 70–75 (2018).

45. C. R. Sandate, A. Szyk, E. A. Zehr, G. C. Lander, A. Roll-Mecak, An allosteric network in spastin couples multiple activities required for microtubule severing. *Nat. Struct. Mol. Biol.* **26**, 671–678 (2019).

46. N. Puri, A. W. Karzai, HspQ functions as a unique specificity-enhancing factor for the AAA+ Lon protease. *Mol. Cell* **66**, 672–683.e74 (2017).

47. Y. C. Kim, A. Snoberger, J. Schupp, D. M. Smith, ATP binding to neighbouring subunits and intersubunit allosteric coupling underlie proteasomal ATPase function. *Nat. Commun.* **6**, 8520 (2015).

48. D. M. Smith, H. Fraga, C. Reis, G. Kafri, A. L. Goldberg, ATP binds to proteasomal ATPases in pairs with distinct functional effects, implying an ordered reaction cycle. *Cell* **144**, 526–538 (2011).

49. E. Gur, R. T. Sauer, Recognition of misfolded proteins by Lon, a AAA(+) protease. *Genes Dev.* **22**, 2267–2277 (2008).

50. H. Besche, N. Tamura, T. Tamura, P. Zwickl, Mutational analysis of conserved AAA+ residues in the archaeal Lon protease from Thermoplasma acidophilum. *FEBS Lett.* **574**, 161–166 (2004).

51. A. S. Menon, A. L. Goldberg, Binding of nucleotides to the ATP-dependent protease La from Escherichia coli. *J. Biol. Chem.* **262**, 14921–14928 (1987).

52. M. L. Wohlever, T. A. Baker, R. T. Sauer, Roles of the N domain of the AAA+ Lon protease in substrate recognition, allosteric regulation and chaperone activity. *Mol. Microbiol.* **91**, 66–78 (2014).

53. M. Li, A. Gustchina, F. S. Rasulova, E. E. Melnikov, M. R. Maurizi, T. V. Rotanova, Z. Dauter, A. Wlodawer, Structure of the N-terminal fragment of Escherichia coli Lon protease. *Acta Crystallogr. D Biol. Crystallogr.* **66**, 865–873 (2010).

54. C. Bieniossek, B. Niederhauser, U. M. Baumann, The crystal structure of apo-FtsH reveals domain movements necessary for substrate unfolding and translocation. *Proc. Natl. Acad. Sci. U.S.A.* **106**, 21579–21584 (2009).

55. T. V. Rotanova, I. Botos, E. E. Melnikov, F. Rasulova, A. Gustchina, M. R. Maurizi, A. Wlodawer, Slicing a protease: Structural features of the ATP-dependent Lon proteases gleaned from investigations of isolated domains. *Protein Sci.* **15**, 1815–1828 (2006).

56. J. Patterson-Ward, J. Tedesco, J. Hudak, J. Fishovitz, J. Becker, H. Frase, K. McNamara, I. Lee, Utilization of synthetic peptides to evaluate the importance of substrate interaction at the proteolytic site of *Escherichia coli* Lon protease. *Biochim. Biophys. Acta* **1794**, 1355–1363 (2009).

57. S. C. Su, C. C. Lin, H. C. Tai, M. Y. Chang, M. R. Ho, C. S. Babu, J. H. Liao, S. H. Wu, Y. C. Chang, C. Lim, C. I. Chang, Structural basis for the magnesium-dependent activation and hexamerization of the Lon AAA+ protease. *Structure* **24**, 676–686 (2016).

58. C. Gatsogiannis, D. Balogh, F. Merino, S. A. Sieber, S. Raunser, Cryo-EM structure of the ClpXP protein degradation machinery. *Nat. Struct. Mol. Biol.* **26**, 946–954 (2019).

59. C. W. Chang, S. Lee, F. T. F. Tsai, Structural elements regulating AAA+ protein quality control machines. *Front. Mol. Biosci.* **4**, 27 (2017).

60. A. L. Yokom, S. N. Gates, M. E. Jackrel, K. L. Mack, M. Su, J. Shorter, D. R. Southworth, Spiral architecture of the Hsp104 disaggregase reveals the basis for polypeptide translocation. *Nat. Struct. Mol. Biol.* **23**, 830–837 (2016).

61. A. Heuck, S. Schitter-Sollner, M. J. Suskiewicz, R. Kurzbauer, J. Kley, A. Schleiffer, P. Rombaut, F. Herzog, T. Clausen, Structural basis for the disaggregase activity and regulation of Hsp104. *eLife* **5**, e21516 (2016).

62. J. Patterson-Ward, J. Huang, I. Lee, Detection and characterization of two ATP-dependent conformational changes in proteolytically inactive Escherichia coli Lon mutants by stopped flow kinetic techniques. *Biochemistry* **46**, 13593–13605 (2007).

63. D. Vineyard, J. Patterson-Ward, A. J. Berdis, I. Lee, Monitoring the timing of ATP hydrolysis with activation of peptide cleavage in *Escherichia coli* Lon by transient kinetics. *Biochemistry* **44**, 1671–1682 (2005).

64. J. A. Kenniston, T. A. Baker, R. T. Sauer, Partitioning between unfolding and release of native domains during ClpXP degradation determines substrate selectivity and partial processing. *Proc. Natl. Acad. Sci. U.S.A.* **102**, 1390–1395 (2005).

65. E. J. Enemark, L. Joshua-Tor, Mechanism of DNA translocation in a replicative hexameric helicase. *Nature* **442**, 270–275 (2006).

66. Y. Dong, S. Zhang, Z. Wu, X. Li, W. L. Wang, Y. Zhu, S. Stoilova-McPhie, Y. Lu, D. Finley, Y. Mao, Cryo-EM structures and dynamics of substrate-engaged human 26S proteasome. *Nature* **565**, 49–55 (2019).

67. M. E. Matyskiela, G. C. Lander, A. Martin, Conformational switching of the 26S proteasome enables substrate degradation. *Nat. Struct. Mol. Biol.* **20**, 781–788 (2013).

68. M. A. Herzik Jr., M. Wu, G. C. Lander, Achieving better-than-3-Å resolution by single-particle cryo-EM at 200 keV. *Nat. Methods* **14**, 1075–1078 (2017).

69. C. Suloway, J. Pulokas, D. Fellmann, A. Cheng, F. Guerra, J. Quispe, S. Stagg, C. S. Potter, B. Carragher, Automated molecular microscopy: The new Leginon system. *J. Struct. Biol.* **151**, 41–60 (2005).

70. G. C. Lander, S. M. Stagg, N. R. Voss, A. Cheng, D. Fellmann, J. Pulokas, C. Yoshioka, C. Irving, A. Mulder, P. W. Lau, D. Lyumkis, C. S. Potter, B. Carragher, Appion: An integrated, database-driven pipeline to facilitate EM image processing. *J. Struct. Biol.* **166**, 95–102 (2009).

71. S. Q. Zheng, E. Palovcak, J. P. Armache, K. A. Verba, Y. Cheng, D. A. Agard, MotionCor2: Anisotropic correction of beam-induced motion for improved cryo-electron microscopy. *Nat. Methods* **14**, 331–332 (2017).

72. A. Rohou, N. Grigorieff, CTFFIND4: Fast and accurate defocus estimation from electron micrographs. *J. Struct. Biol.* **192**, 216–221 (2015).

73. N. R. Voss, C. K. Yoshioka, M. Radermacher, C. S. Potter, B. Carragher, DoG Picker and TiltPicker: Software tools to facilitate particle selection in single particle electron microscopy. *J. Struct. Biol.* **166**, 205–213 (2009).

74. A. M. Roseman, FindEM—A fast, efficient program for automatic selection of particles from electron micrographs. *J. Struct. Biol.* **145**, 91–99 (2004).

75. S. H. Scheres, RELION: Implementation of a Bayesian approach to cryo-EM structure determination. *J. Struct. Biol.* **180**, 519–530 (2012).

76. A. Punjani, J. L. Rubinstein, D. J. Fleet, M. A. Brubaker, cryoSPARC: Algorithms for rapid unsupervised cryo-EM structure determination. *Nat. Methods* **14**, 290–296 (2017).

77. D. Kimanius, B. O. Forsberg, S. H. Scheres, E. Lindahl, Accelerated cryo-EM structure determination with parallelisation using GPUs in RELION-2. *eLife* **5**, e18722 (2016).

78. J. Zivanov, T. Nakane, B. O. Forsberg, D. Kimanius, W. J. Hagen, E. Lindahl, S. H. Scheres, New tools for automated high-resolution cryo-EM structure determination in RELION-3. *eLife* **7**, e42166 (2018).

79. E. F. Pettersen, T. D. Goddard, C. C. Huang, G. S. Couch, D. M. Greenblatt, E. C. Meng, T. E. Ferrin, UCSF Chimera—A visualization system for exploratory research and analysis. *J. Comput. Chem.* **25**, 1605–1612 (2004).

80. D. Tegunov, P. Cramer, Real-time cryo-electron microscopy data preprocessing with Warp. *Nat. Methods* **16**, 1146–1152 (2019).

81. A. Waterhouse, M. Bertoni, S. Bienert, G. Studer, G. Tauriello, R. Gumienny, F. T. Heer, T. A. P. de Beer, C. Rempfer, L. Bordoli, R. Lepore, T. Schwede, SWISS-MODEL: Homology modelling of protein structures and complexes. *Nucleic Acids Res.* **46**, W296–W303 (2018).

82. P. Emsley, B. Lohkamp, W. G. Scott, K. Cowtan, Features and development of Coot. *Acta Crystallogr. D Biol. Crystallogr.* **66**, 486–501 (2010).

83. P. D. Adams, P. V. Afonine, G. Bunkóczi, V. B. Chen, I. W. Davis, N. Echols, J. J. Headd, L. W. Hung, G. J. Kapral, R. W. Grosse-Kunstleve, A. J. McCoy, N. W. Moriarty, R. Oeffner, R. J. Read, D. C. Richardson, J. S. Richardson, T. C. Terwilliger, P. H. Zwart, PHENIX: A comprehensive Python-based system for macromolecular structure solution. *Acta Crystallogr. D Biol. Crystallogr.* **66**, 213–221 (2010).

84. M. A. Herzik Jr., J. S. Fraser, G. C. Lander, A multi-model approach to assessing local and global cryo-EM map quality. *Structure* **27**, 344–358.e43 (2019).

85. T. D. Goddard, C. C. Huang, E. C. Meng, E. F. Pettersen, G. S. Couch, J. H. Morris, T. E. Ferrin, UCSF ChimeraX: Meeting modern challenges in visualization and analysis. *Protein Sci.* **27**, 14–25 (2018).

86. G. Cardone, J. B. Heymann, A. C. Steven, One number does not fit all: Mapping local variations in resolution in cryo-EM reconstructions. *J. Struct. Biol.* **184**, 226–236 (2013).

87. M. G. Prisant, C. J. Williams, V. B. Chen, J. S. Richardson, D. C. Richardson, New tools in MolProbity validation: CaBLAM for CryoEM backbone, UnDowser to rethink "Waters", and NGL viewer to recapture online 3D graphics. *Protein Sci.* **29**, 315–329 (2019).

88. B. A. Barad, N. Echols, R. Y. Wang, Y. Cheng, F. DiMaio, P. D. Adams, J. S. Fraser, EMRinger: Side chain-directed model and map validation for 3D cryo-electron microscopy. *Nat. Methods* **12**, 943–946 (2015).